Measurements of a rotor flow in ground effect and visualisation of the brown-out phenomenon

Nita D. Nathan*
Research Student
nnathan@aero.gla.ac.uk

Richard B. Green
Senior Lecturer
richardg@aero.gla.ac.uk

Department of Aerospace Engineering, University of Glasgow
Glasgow G12 8QQ, United Kingdom

Abstract

Quantitative and qualitative results of a series of experiments conducted on a rotor in ground effect at low forward speeds are presented. The velocity over a wide area of the ground effect wake was measured using Particle Image Velocimetry (PIV), and the evolution of the flow is described as the forward speed increases. Helicopter brown-out was simulated through a series of flow visualisation experiments. The technique involved sprinkling a fine powder on the ground below and ahead of the rotor. This helps to validate the experimental simulation of the brown-out phenomenon. Larger dust clouds were observed at lower advance ratio, and the dust cloud penetrated into the areas of the flow including those where vorticity levels were of low or negligible magnitude.

1. INTRODUCTION

When a helicopter is operating close to the vicinity of the ground, the rotor is said to be in ground effect (IGE). The fluid dynamics of the resulting rotor wake, influenced by the presence of the ground, is significantly different to that of a rotor operating in normal conditions, i.e out of ground effect (OGE). There are various performance advantages IGE, but ground effect (GE) also leads to some operational difficulties. For example, when a helicopter is close to a dusty or sandy ground, the downwash from the rotor system can lift the loose matter off the ground to create a cloud that can envelope the entire aircraft. The consequence of this brown-out is that the pilot may lose all visual cues and become disoriented. The loss of a significant number of helicopters has been attributed to this over the years; American defence sources suggest some 21 MH-53 and 10 HH-60G brown-out mishaps since 1973 (source www.defenseindustrydaily.com).

Many discussions of GE have considered the benefits due to GE on thrust or power. Performance related experiments on rotor IGE flow have commanded the most interest as it has been observed that the power required to hover IGE is significantly lower than OGE [1, 2, 3, 4]. This power reduction, observed experimentally on numerous occasions [3, 5, 6], has been confirmed to exist up to a ground height (i.e. ratio of the height h above the ground to the rotor diameter D, $\frac{h}{D}$) of around 1, after which the ground is not seen to have any significant effect on the rotor *performance*. This has in turn piqued research interests in both mathematical and computational modelling of rotor IGE performance [6, 7, 4]. The most obvious difference in the wake of a hovering rotor IGE is the expansion of the wake instead of the classical contraction seen OGE [4]. The PIV plot in Figure 1 highlights the differences observed between an OGE and IGE wake of a hovering rotor. Less obvious is a region of 'dead-air' or no-flow, identified as the cause of the spreading of the rotor wake IGE [2]. In addition, velocity distribution experiments show that the dead-air region possesses a low negative (upwash) velocity instead of the positive velocities associated with the rotor downwash. It is conceptually easy to see that the brown-out phenomenon in hover at least is due to the manner in which the tip vortices pass over the ground and pick up loose material, and then how this material is advected, but detailed knowledge of the flow field is required.

The majority of rotor IGE experimental research has concentrated on the low advance ratio ($\mu = \frac{U_\infty}{V_{tip}}$) forward flight case, where U_∞ is the forward flight speed and V_{tip} is the rotor blade tip velocity. While most of this research was done to analyse the performance implications of the ground on a rotor operating at low advance ratio [4], limited quantitative analysis have been done to determine the wake characteristics at this operating conditions. In forward flight GE, two major ground effect flow features have been observed; a recirculation loop at very low advance ratio and a ground vortex at higher advance ratio [8]. The flight regimes are best expressed in terms of the normalised advance ratio given by $\mu^* = \frac{\mu}{\sqrt{C_T/2}}$, where C_T is the hover thrust coefficient, and have been broadly defined by Curtiss *et. al* [3, 5]. The recirculation regime is observed to occur at $0.4 < \mu^* < 0.7$, with a recirculation loop observed ahead of the rotor disk. This loop is seen to possess 7-8 tip vortices and is observed along the longitudinal plane

*Presented at the American Helicopter Society 64th Annual Forum, Montréal, Canada, April 29 - May 1, 2008.

(a) Hover OGE

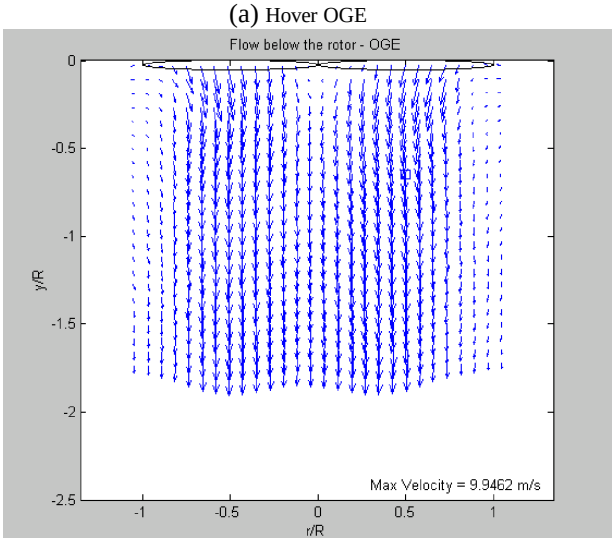

(b)Hover IGE

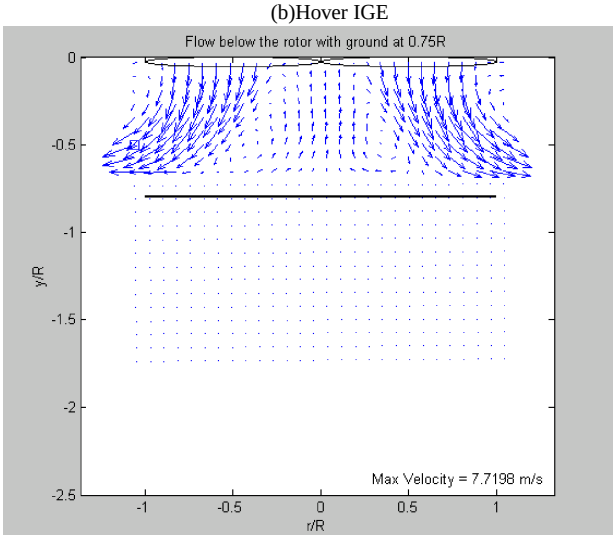

Figure 1: Comparison between OGE and IGE wake of a hovering rotor. The figure shows PIV velocity plots of the mean flow of a rotor hovering at different heights above the ground.

of symmetry [9], occupying a significant portion of the flow field ahead of the rotor leading edge [5]. The recirculation loop has been observed to increase the inflow through the forward portion of the rotor [10]. A schematic diagram of this is shown in figure 2(a). The tip vortices pass along the ground ahead of the rotor and then move in an arc upwards and back towards the rotor disk, where reports suggest a re-ingestion through the rotor disk [11]. This demands the formation of a topological separation point on the ground some distance ahead of the rotor. This recirculation pattern is seen to disappear with increasing μ. Using hot-wire anemometry, with the rotor at a particular height, Saijo *et. al* observed the separation point to oscillate about a point, between $0.04 < \mu < 0.06$, after which it appeared to be stable ($0.06 < \mu < 0.1$), all the while moving towards the rotor to form the ground vortex regime [11]. Successful computation of these forward flight regimes has been achieved by Brown and Whitehouse [7].

Surface flow visualisation experiments, conducted by Boyd *et. al* [12] using smoke and tufts on the ground indicate the presence of an interaction boundary on the ground when in forward flight. The interaction boundary is formed as the wake from the rotor encounters the oncoming free-stream. The boundary is seen to move towards the rotor as the free-stream velocity increases. The symmetry of the interaction boundary depends on the rotor used. If the rotor is rigid, the inability for the rotor to compensate for the differential lift produced in the advancing and retreating sides of the rotor, would result in the formation of an asymmetric interaction boundary on the ground. This boundary is otherwise symmetric and parabolic in shape, if the rotor is allowed to trim or during hover [13].

At around $\mu^* > 0.7$, a well-defined concentrated horse-shoe vortex is seen to form [3]. The formation of this ground vortex (GV) is generally noted to be the function of μ, blade collective pitch and ground height [14]. Flow visualisations done by Sheridan and Wiesner, suggest that the ground vortex is formed as the spreading wake ahead of the rotor disk is decelerated and stopped by the free-stream, causing the flow along the ground to separate and roll up (refer to figure 2(b)) [8]. Increments in μ results in the GV gaining prominence, with part of the freestream being entrained into the ground vortex and part of it being ingested into the rotor. This additional inflow through the rotor is thought to increase the power required by the rotor, reducing the performance benefits experienced by the rotor in hover GE [4]. The GV is seen to move towards the rotor as μ is further increased. When the GV is just beneath the leading edge of the rotor, the inflow through the rotor, induced by the GV is at its maximum, as seen in figure 2(c). The power required during this stage is as much as, or just below the power required OGE, as identified during performance analysis. The GV continues to move further downstream, away from the leading edge of the rotor disk, with increasing μ. This movement reduces the inflow through the rotor disk, as can be seen from figure 2(d), and also results in some amount of upflow through the disk [8], reducing the power required compared to when the GV was just below the leading edge of the rotor disk. As the GV continues to move further downstream, it is seen to lose its strength and diminish in size, eventually disappearing from the wake as the advance ratio, reaches $\mu = 0.12$ [14] or around $\mu^* = 1.3$. A Particle Image Velocimetry investigation of the GV regime, conducted by Ganesh and Komerath, showed the influence of the tip vortex system on the formation of the GV [15] . The strengths and locations of the GV at particular advance ratios were analysed. The GV was seen to possess strengths exceeding the vorticity strengths of the tip vortices which were seen to be ingested to form the GV. Discrete tip vortices were also seen to be present within the GV.

The forward flight IGE flow field is therefore far more complicated than the hover IGE flow, but it immediately appears that brown-out must again be due to the action on the ground of the vortex system trailed below the rotor and the subsequent behaviour of the material that is swept up forward of the ro-

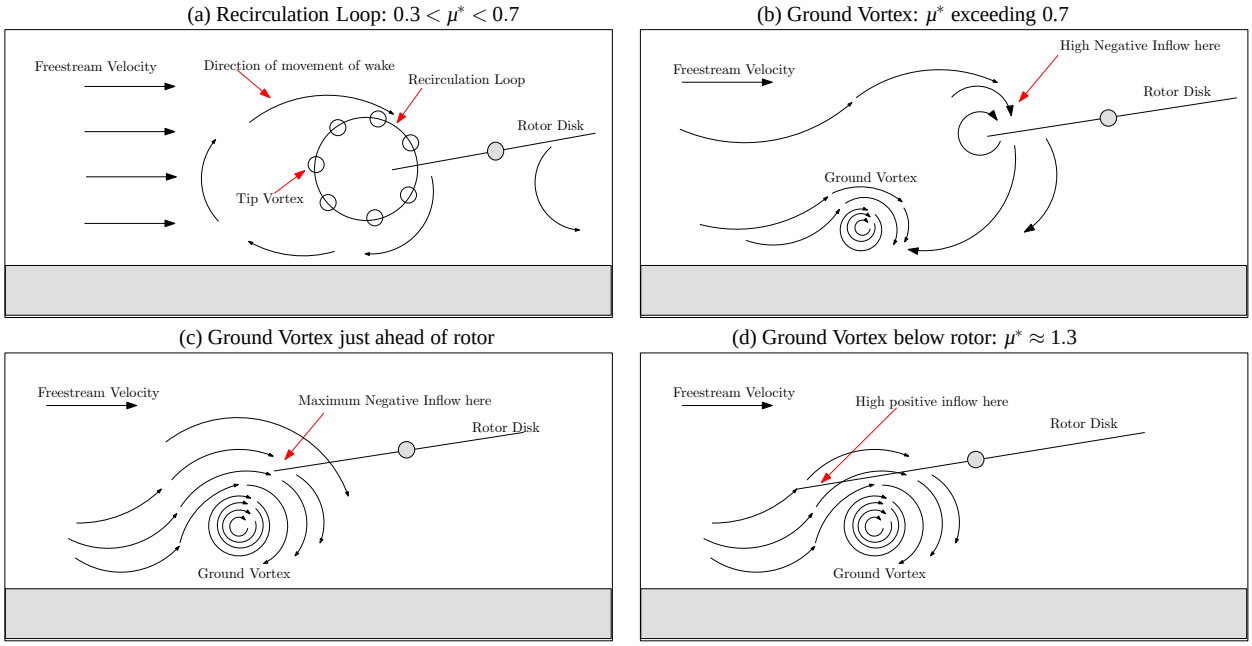

Figure 2: Schematic of the ground effect flow at varying advance ratios [8]. The recirculation regime is shown in frames (a) and (b) and the ground vortex regime in frames (c) and (d).

tor. What appears to be lacking in the background literature is detailed knowledge of the IGE flow field in forward flight. Improved understanding of the flow field is a necessary pre-cursor to gaining knowledge of the brown-out.

2. EXPERIMENTAL METHODS

2.1. Rotor Rig

Two different wind tunnel facilities were used during the course of the GE and brown-out investigations. Due to the limitations imposed by the physical dimensions of the wind tunnel facilities available and the huge spatial extent of the ground effect wake, it was necessary to use a very small-scale rotor system for these investigations. The main issue of concern regarding the fluid dynamics is the circulation Reynolds number $\frac{\Gamma}{\nu}$, where Γ is the trailing vortex circulation. As long as this value is above a moderate value of some 10000 or so, then the wake behaviour will be representative of that of a much larger rotor system.

The rotor rig that was used for these investigations was based on readily available propellers designed for model aircraft. These propellers are designed to produce a useful vortex wake that is representative of a helicopter rotor wake in that it consists of inter-twined, helical vortices, and hence were deemed suitable for use in an experimental rotor rig. Although these propellers are highly twisted, some modern helicopter main rotors do have large amounts of twist.

For the purposes of these experiments, a two-bladed model propeller, manufactured by Graupner was used. It is not clear what aerofoil section(s) are used for these propellers, although they are cambered. The propellers were fixed onto the shaft of a small d.c. electric motor capable of spinning the rotor at a rate of 120Hz (speed controlled simply by increasing the supply voltage). The rotor speed was monitored using a stroboscope, and the thrust was measured by mounting the motor on a 0.6kg load-cell. This assembly was fixed to the end of a long sting attached to a hand-cranked vertical traverse unit, which was placed on the ground so that the rotor disk was nominally in the horizontal plane with the motor above the disk. A schematic diagram of the apparatus is shown in Figure 3 and information of the model rotor used is given in Table 1.

Rotor	Dimensions
Pitch	7.5cm
Hub diameter	1.5cm
Blade tip	Square-cut tip
Root Chord	1.05cm
Tip Chord	0.8cm
Max Chord	1.46cm at 50% outboard of root
Max Thickness Ratio	16.4% at 50% outboard of root

Table 1: Rotor Dimensions

2.2. Wind Tunnel Facilities

Quantitative investigations of the GE wake, using PIV, were conducted in the Anatomy Wind Tunnel of the University of Glasgow's Aerospace Department. This is a $1.05\text{m} \times 0.85\text{m}$ octagonal working section, closed return tunnel, capable of a top speed of some 30ms^{-1} and a contraction ratio of 9:1. A raised ground board had to be placed into this tunnel due to its limited optical access. Flow visualisation of the brown-out phenomenon was conducted in the Smoke Tunnel of the department. The Smoke Tunnel has a $0.91\text{m} \times 0.91\text{m}$ square, 4m long working section. This is a closed, non-return type tunnel, with

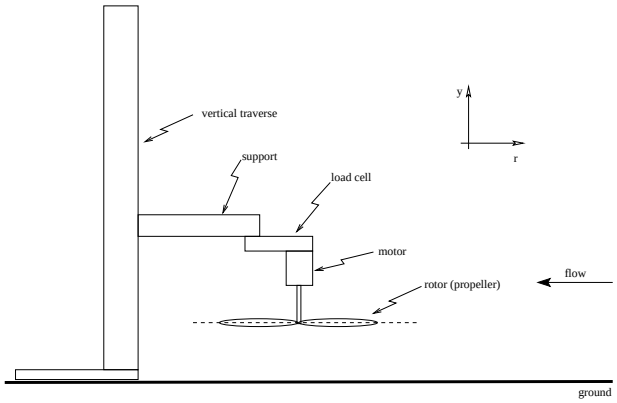

Figure 3: Schematic diagram of rotor system, motor, load-cell and vertical traverse. The sense of the (r,y) coordinate system is shown, but its origin is at the centre of the rotor.

a settling chamber and 9:1 contraction at the upstream end and a fan at the downstream end. The maximum speed of the tunnel is some 2.5ms^{-1}. Flow visualisation is achieved by injecting smoke or some other seeding medium into the air flow at the desired location, and a flood lamp, flash lamp or 5W, continuous wave (CW) laser can be used for illumination of the required region of the flow. Filters downstream of the fan remove the seeding medium from the air. For the brown-out testing in this tunnel, the rotor assembly is simply placed on the floor of the tunnel.

2.3. Rotor IGE experiments

Quantitative analysis of the wake of the rotor IGE forward flight was done in the Anatomy Wind Tunnel using both two-dimensional (2D) PIV and Stereoscopic (Stereo) PIV. 2D PIV allows for the measurement of the *(u,v)* velocity components of the flow field while Stereo PIV allows for the third velocity component *(w)* to be measured for an area of the flow. The GE experiments were conducted for a range of ground heights of $\frac{\text{h}}{\text{D}} = 0.25$ to $\frac{\text{h}}{\text{D}} = 1.0$ and normalised advance ratios of $\mu^\star = 0.3$ to $\mu^\star = 1.3$. During the experiments, the rotor was operated at a speed of 94Hz, with a measured thrust coefficient, $\text{C}_\text{T} = 0.14$. The normalised advance ratio for various test cases were achieved by varying the wind tunnel speed accordingly.

The PIV system used in the forward flight test runs has been employed in a range of rotor flow tests in the past. For the 2D PIV, a Kodak MegaPlus ES1.0 digital video camera, with a 1018×1008 pixel CCD chip, fitted with a 50mm focal length Nikkor lens set to $f/2.4$, was used to record a suitable region of the flow. The camera was placed normal to the object plane with the region of interest, illuminated by a light sheet produced by a Spectra-Physics Lab130-10 Nd:YAG single cavity, double pulsed, frequency doubled laser, with a wavelength of 532nm and a pulse duration of 8*ns*. The light sheet, of approximately 2mm thickness, was aligned along the longitudinal axis of the tunnel, to illuminate the region upstream of the rotor axis. Seeding was produced using a smoke generator that heats smoke oil to produce a fine oil mist; the manufacturer claims a nominal smoke particle diameter of 0.2μm. Image capture was done using a National Instrument PCI-1424 digital frame grabber operated using LABVIEW. The laser, camera control and image capture systems were all synchronised using a National Instruments PCI-TI0-10 counter timer card and controlled by a single computer.

In the case of the Stereo PIV, two Kodak MegaPlus ES1.0 digital video cameras, fitted with 50mm lenses were used to record the flow. The cameras were arranged in the angular displacement Stereo PIV system, to allow for greater measurement accuracy of the out-of-plane *(w)* velocity component [16]. The camera lens planes were aligned with perspective angles of 21.04^o and -22.3^o from the normal of the object plane, to capture the wake in the longitudinal plane ahead of the rotor hub. All the other experimental details used for the Stereo PIV setup were similar to that of the 2D PIV case. The optical arrangement for both the PIV setups, allowed for an $18\text{cm} \times 18\text{cm}$ square field of view of the flow to be recorded. Scaled in terms of the rotor diameter, this amounts to a one diameter square area field of view. Different upstream positions of the rotor wake were recorded by moving the rotor with respect to the camera field of view. In cases where the GE wake was seen to extend further than the one diameter field of view, a higher resolution Kodak MegaPlus MP4 digital video camera, with a 2048×2048 pixel CCD chip, was used. This camera allowed for wider field of views to be captured, with no compromise to the resolution of the velocity vector maps derived from the camera images. This camera was used especially with the lower advance ratio cases, where the wake was seen to spread beyond one diameter from the rotor leading edge.

Double frame, double exposure PIV was used for both the 2D and stereo PIV tests. In this method, two images, separated by a known time delay, Δt is taken. A calibration, done before the actual PIV, provides a transfer function, used to convert the pixel displacements on the image into physical displacements of the flow. These displacements, together with the time delay set, are then used to obtain quantitative information such as velocity, of the recorded flow field [17]. For each GE test, 300 image pairs, with a set time delay of $90\mu s$, were taken. Analysis of the images, by successive cross-correlation and Lagrangian tile-shifting produces high-resolution velocity vector maps. Spatial resolution of the measurements is clearly dictated by the field of view, but for the current experiments, where the field of view

was around one rotor diameter square, the effective measurement area per point was around $0.016\text{D} \times 0.016\text{D}$.

2.4. Brown-out Flow Visualisation

The simulation of the brown-out phenomenon required the use of appropriate seeding particles to ensure that the conditions are represented well in the experiments. For the purposes of these tests, talcum powder was used as seeding because of its ability to simulate the basic dust dynamics and also for safety. The talcum powder was introduced into the flow by spreading it along the floor of the wind tunnel just below the rotor. At the rotor speed and wind tunnel speed setting used, it was observed that the talcum powder was lifted off the ground by the action of the rotor induced flow alone. The wind tunnel speed alone could not do this, and this is important given that the forward flight was simulated by the wind tunnel flow. As the talcum powder depleted during the experiment, it was essential that the camera photography was done as soon as possible after the rotor was switched on.

A Mikrotron MotionBlitz high-speed digital video camera was used for the flow visualisation experiments to permit visualisation of the tip vortices moving over the ground. This camera was capable of recording at a frame rate of 500Hz at a full-frame resolution of $1\text{k} \times 1\text{k}$ pixels, and was used with a 5W laser. This camera was fitted with a range of Nikon lenses to suit the field of view and the amount of illumination available. The brown-out visualisation was carried out for $\mu^* = 0.37$ and $\mu^* = 0.6$ at ground distances of a quarter and half a diameter. Unlike in the Anatomy tunnel, the higher normalised advance ratios were unachievable in this tunnel. Thus, the rotational speed of the rotor had to be altered accordingly to allow for the required normalised advance ratio, with C_T held constant at $C_T = 0.14$.

3. RESULTS

3.1. PIV Analysis of the GE flow field

PIV is a non-intrusive technique for measuring velocity over a wide area of the flow field in a near instant. It is particularly advantageous for the investigation of unsteady flows since the vorticity is readily obtained from a single snapshot of the velocity field. Statistics of the unsteady flow can also be calculated if a sufficiently large number of velocity fields are captured. The field of view chosen for the PIV analysis, the choice of time delay, the seeding density and the thickness of the light sheet combine to produce a high resolution velocity map of excellent fidelity. The PIV here is used to determine the (u,v) velocity field in the (r,y) plane.

Streamlines and vorticity ($\omega = \frac{\partial v}{\partial r} - \frac{\partial u}{\partial y}$) constructed from the mean velocity for $\mu^* = 0.65$ and $\mu^* = 0.3$ with the rotor at a ground distance of half a diameter are shown in Figure 4. The streamlines are obtained from the averaged velocity field from the PIV data for that case; seed points are placed at selected locations in the velocity field, and the streamlines are formed by tracing a particle released from each seed point. These flow patterns are only cartoons; the flow is three-dimensional and unsteady, so no streamline pattern like those to be presented would ever be observed, but they are a useful aid in interpreting the results. The vorticity has been scaled with $\frac{V_h}{R}$, where $V_h = V_{tip}\sqrt{\frac{C_T}{2}}$ is the hover induced velocity. The rotor tip is at the ordinate $(r/R, y/R) = (1,0)$, and the ground is along $y/R = -1$.

For a rotor ground height of half a diameter, with $\mu^* = 0.65$, Figure 4(b) shows a region of low positive vorticity present at about 1.5R away from the rotor hub extending to a height of $\frac{y}{R} = 0.2$. A comparison of this to the vorticity plot of $\mu^* = 0.3$, in Figure 4(d), shows the region of low positive vorticity at around 3.5R away from the rotor hub extending to $\frac{y}{R} = 0.6$. The spread of the GE wake at this advance ratio was too wide to be captured within the field of view of the PIV plot. A segment of the wake, as shown in Figure 4(d), shows the extent of the spread of the wake at $\mu^* = 0.3$. The wake starts at the rotor leading edge as a thin ribbon of high vorticity reaching heights of $\frac{y}{R} = -0.2$[1]. As it reaches a ground distance of around 2.0R, this ribbon is seen to expand to a relatively large region of low positive vorticity, spreading to about 4.5R.

The PIV results indicated that as μ^* increases, the region of positive vorticity is seen to form nearer the rotor disk, with increased strength and a more compact size. This eventually becomes a vortex of high strength just under the leading edge of the rotor disk at a particular μ^*. At a ground distance of half a diameter, this transition was observed to occur at $\mu^* = 0.9$. At this ground distance, the vorticity magnitude within the region of positive vorticity was seen to increase with μ^*, reaching a peak value at $\mu^* = 0.9$, then reducing as μ^* is further increased. Figures 5(b) and 5(d) show the concentrated vortex form under the rotor disk after $\mu^* = 0.9$. The figures, show the high strength vortex just under the rotor disk leading edge in Figure 5(b), possessing greater strength than the vortex located closer to the rotor hub in Figure 5(d) at the higher μ^* value. The figures also indicate the skewed root and tip vortex system generated by the rotor operating at these flight speeds. The above-mentioned trend is seen to be representative of the ground effect flow field at the various ground distances tested. Variations in ground distance of the rotor is seen to displace the location of the region of positive vorticity for the range of forward flight speeds tested. A reduction in the ground distance is seen to displace the region of vorticity towards the right, with the opposite effect observed at higher ground distances. Figures 6(a) and 6(b) compare the location of the region of vorticity for the same forward flight speed of $\mu^* = 0.7$, at ground distances of half a diameter and a quarter of a diameter. Figure 6(a) shows the vorticity centroid located at $\frac{r}{R} \approx 1.6$, whereas this is located at $\frac{r}{R} \approx 2$, in Figure 6(b). The vorticity strengths of these regions have been observed to be comparable despite the differences in their locations.

The different regimes of the GE flow field, identified from previous research [3, 9] can be distinguished from the PIV vorticity plots obtained. At a ground distance of half a diameter, the recirculation regime was identified to exist between $\mu^* = 0.6$ and $\mu^* = 0.9$, while the GV regime was seen to exist between $\mu^* = 0.9$ and $\mu^* = 1.2$. Higher than this advance ratio, no vortex is observed to form. At the higher ground distance cases tested, these μ^* ranges were seen to decrease, with the GV regime occuring at lower μ^* values.

[1] not presented

$\mu^* = 0.65$: (a) mean flow streamlines

(b) vorticity from mean flow

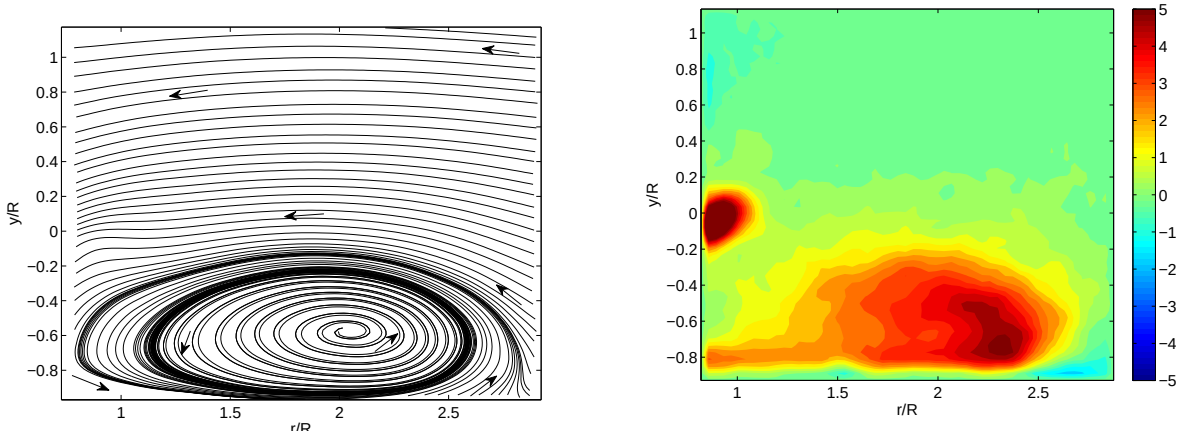

$\mu^* = 0.3$: (c) mean flow streamlines

(d) vorticity from mean flow

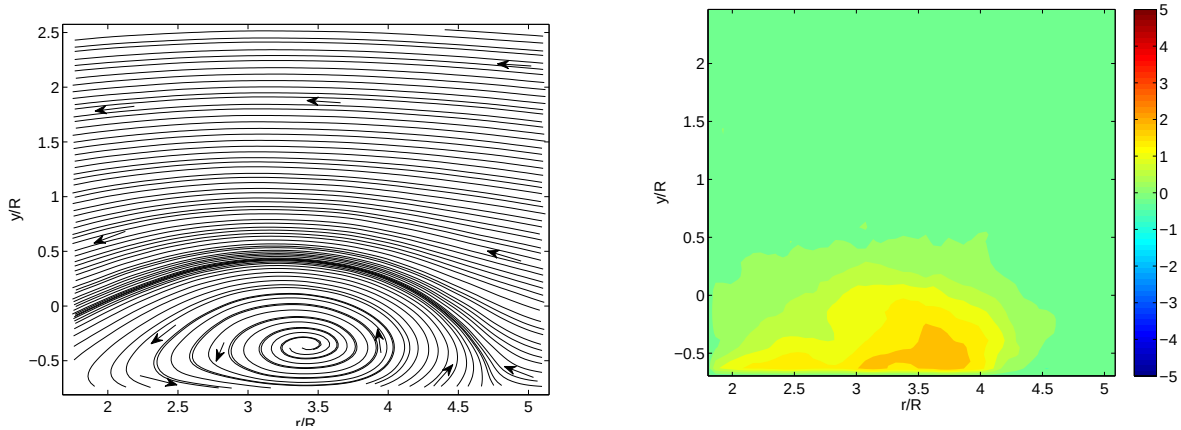

Figure 4: Mean flow streamlines and mean non-dimensional vorticity from PIV for the rotor at 0.5D above the ground for $\mu^* = 0.65$ (frames (a) and (b)) and $\mu^* = 0.3$ (frames (c) and (d)). For (a) and (b) the field of view is just ahead of the edge of the rotor disk, while for (c) and (d) the field of view is about 1D upstream. The images in frames (c) and (d) are obtained using a higher resolution camera to capture the spread of the wake at this low μ^*.

$\mu^* = 0.9$: (a) mean flow streamlines

(b) vorticity from mean flow

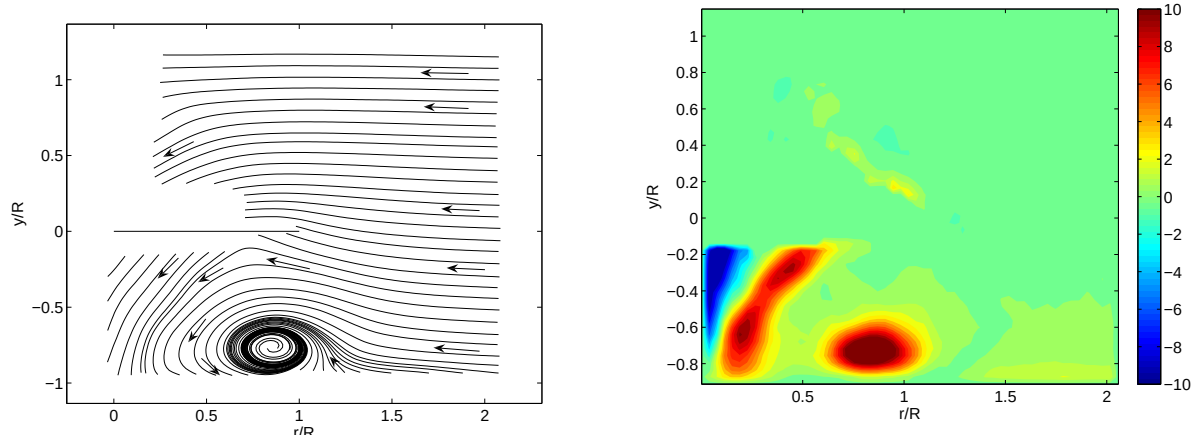

$\mu^* = 1.1$: (c) mean flow streamlines

(d) vorticity from mean flow

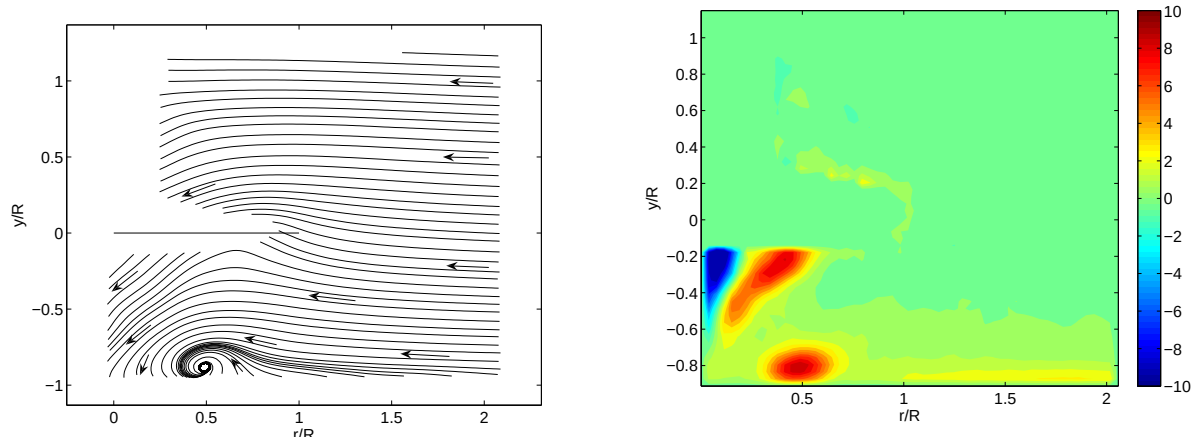

Figure 5: Mean flow streamlines and mean non-dimensional vorticity from PIV for the rotor at 0.5D above the ground for $\mu^* = 0.9$ (frames (a) and (b)) and $\mu^* = 1.1$ (frames (c) and (d)). For all frames, the field of view is just below the rotor disk.

$\mu^* = 0.7$: (a) mean vorticity at 0.5D

(b) mean vorticity at 0.25D

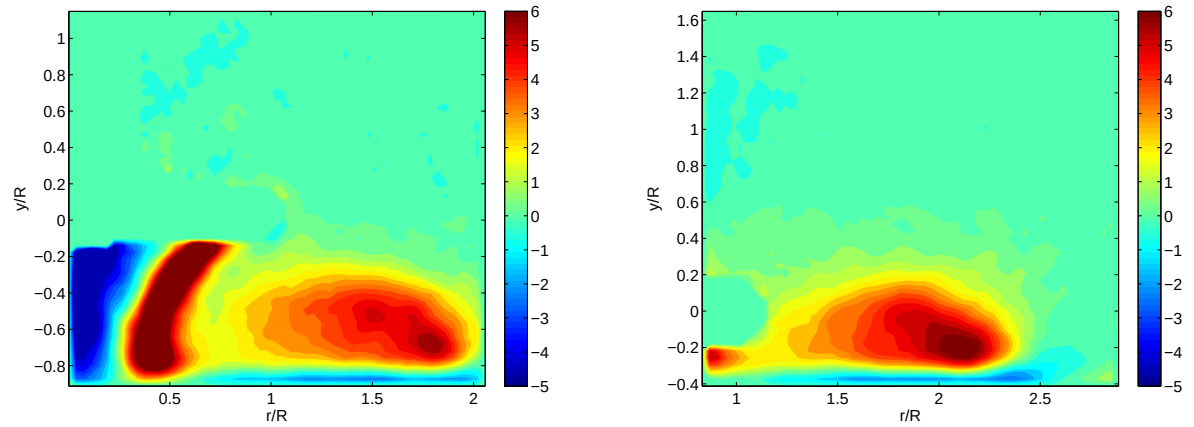

Figure 6: Mean non-dimensional vorticity from PIV for the rotor at 0.5D and 0.25D above the ground for $\mu^* = 0.7$. For frame (a), the field of view is under the rotor disk while the field of view is just ahead of the rotor disk for frame (b).

The presence of tip vortices (TVs) around the recirculation loop is visible in the individual vorticity plots obtained from the PIV [9]. Figure 7(a) show the TVs, represented as small regions of high positive vorticities trailed along the ground and uplifted to form a loop-like structure. The presence of the TVs in the flow field are not visible in the mean vorticity plots due to the averaging process of the individual PIV images. This removes the unsteady features in the flow field, leaving only the gross features. The individual vorticity plots also provide an indication of the true magnitudes of vortex strengths experienced within the fields of view observed at an instant of time.

Individual vorticity plots from the recirculation regimes, show the TVs leave the ground at the separation point and initially head back towards the rotor. The TVs are then observed to either accumulate around the recirculation region and merge ahead of the rotor disk, or move toward the rotor to be re-ingested[2]. The accumulation of TVs at $\mu^* = 0.65$, at a ground distance of half a diameter, is shown in Figure 7(a). This accumulation is seen to occur around the region identified in Figure 4(b) as the location of the region of positive vorticity. An example of the re-ingestion of the TVs through the rotor is implied in Figure 7(b). The re-ingestion process is observed to be inconsistent at this particular advance ratio, at this ground height. The accumulation process of the TVs ahead of the rotor disk is more prominent, with very few images actually showing the re-ingestion process. Most of the vorticity plots actually show a combination of the re-ingestion and accumulation of the TVs, similar to Figure 7(a), where traces of the TVs are seen to be present near the rotor disk and accumulating around a small region ahead of the rotor. As the advance ratio increases, the re-ingestion process becomes more significant, until the GV regime is reached. The re-ingestion process is also observed to be more prominent at the recirculation regimes at lower ground distances as shown in Figure 8. The significant differences observed from the individual vorticity plots of the recirculation flow regime, as observed from Figures 7(a) and 7(b) indicate the inherent unsteadiness of the recirculation flow regime.

The GV regime, shown in Figures 5(b) and 5(d), is observed to be more stable than the recirculation regime with the separation point at a relatively fixed location on the ground. This is unlike the recirculation regime, where the separation point is seen to fluctuate on the ground. The instantaneous vorticity plots hardly vary, with all the plots showing a tightly concentrated vortex present under the rotor.

The individual vorticity plots also reveal the presence of clumps of negative vorticity present in the regions of the flow around the main concentration of positive vorticity. These negative vorticity concentrations are seen to be more prominent for the higher μ^*, corresponding to the recirculation regime and the GV regime. A clear example of this is shown in Figure 7(a), where clumps of negative vorticities are seen to exist around the main region of positive vorticity. The source of this negative vorticity is attributed to secondary separation induced by the TVs trailed from the rotor tip. Again, these negative vorticity clumps are not visible in the mean vorticity plots due to the averaging process. The PIV data presented by Ganesh *et. al* [15] do not show this negative vorticity; this warrants further investigation.

[2] see brown-out investigations later

3.2. Brown-out simulation results

The flow visualisation experiments performed provided a useful means of understanding the brown-out phenomenon as well as track the evolution of the GE flow field. Tests at $\mu^\star = 0.37$ and $\mu^\star = 0.65$ were performed at ground distances of a quarter and half a diameter. A large cloud of dust was seen to form ahead of the rotor disk leading edge, with the cloud at $\mu^\star = 0.37$ further away from the rotor compared to the $\mu^\star = 0.65$ case. Figure 9 shows stills from the video sequences for $\mu^\star = 0.37$ and $\mu^\star = 0.65$, with the rotor half a diameter above the ground. These dust clouds show the tip vortex trajectories and the separation zones on the tunnel floor. The separation zone on Figure 9(a) is shown by the bright, white region on the right side of the image. Figure 9(b) shows the separation point, much less clearly, further to the right than for the higher advance ratio, but the powder is observed to rise far higher above the rotor, and the contamination of the air by the action of the rotor lifting the powder off the ground is greater in coverage. The apparent wavy effect at the ground in each of these images is the powder picked up by the vortices. The tip vortex trajectories in these movie sequences are reminiscent of the schematic diagram shown in Figure 2(a).

A series of snapshots, shown in Figure 10, traces the path of the trailed TVs along the ground at a ground distance of half a diameter, at $\mu^* = 0.65$. Figure 10(a) shows a TV leaving the ground at the separation point, moving into the dust cloud, approaching the rotor blade. Large agglomerations of powder are picked up by the TV as it passes through the separation zone, and these are the large, white particles in the flow to the right of the separation zone; the lighter particles carried by the TV are forced back towards the separation zone by the wind tunnel flow, while the heavier ones land on the ground. As this TV moves back towards the rotor, it is seen to accelerate tip vortices below, moving to the right. This TV is clear in Figure 10(b), and below it, just to its right, another TV next to the ground is indicated. As this 'accelerated' TV moves further to the right, a large amount of powder is ejected out into the flow to the right the separation zone, an example of which, is shown in Figure 10(c). This TV, when leaving the ground at the separation zone is observed to carry more dust with it. The heavier dust particles are eventually seen to be ejected to the right of the separation zone, while the lighter particles are seen to be carried round by the TV (Figure 10 (d)). The dust carried by the TV follows the trajectory of the TV, and is picked up by the freestream and transported back towards the rotor. The result of this process is an accumulation of dust particles around the area between the rotor tip and the separation zone as more of the TVs enter the flow field, causing an increase in the dust cloud size.

Like the observations made from the PIV, the TVs leaving the separation zone, carrying the dust picked up from the ground, are seen to mainly follow two paths. Some of the TVs are seen to remain ahead of the rotor disk and accumulate at the dust cloud. These accumulating TVs, as described in Figure 10, are observed to cause the TVs on the ground to accelerate. Some of the accelerated TVs on the ground are seen to tuck under the preceding ones (trailing vortices are known

$\mu^* = 0.65$: (a) Accumulation of TVs (b) Re-ingestion of TVs

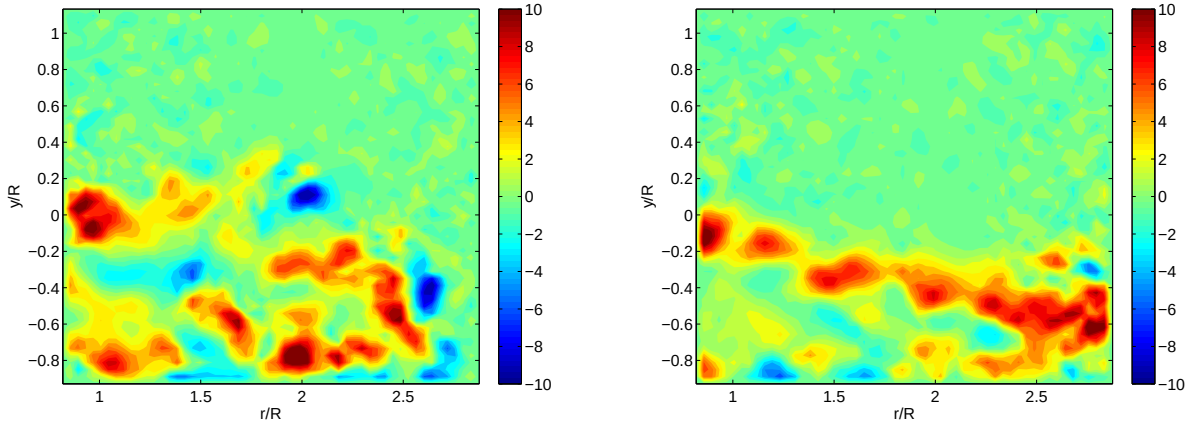

Figure 7: Instantaneous vorticity plots from PIV for the rotor at 0.5D above the ground for $\mu^* = 0.65$. Frame (a) shows the accumulation of the TVs ahead of the rotor while frame (b) shows the re-ingestion of the TVs through the rotor.

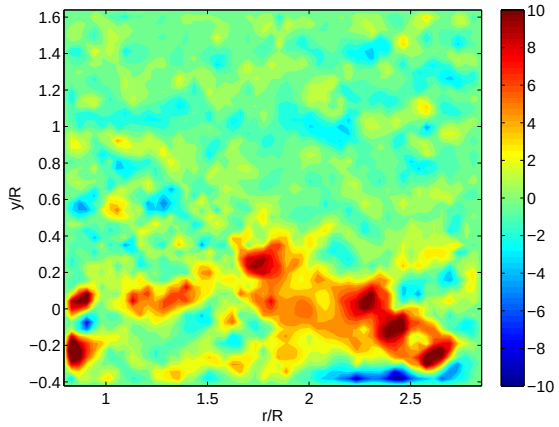

Figure 8: Instantaneous vorticity plot showing the re-ingestion of the TVs at a ground distance of 0.25D for $\mu^* = 0.65$.

(a) $\mu^* = 0.65$ at 0.5D

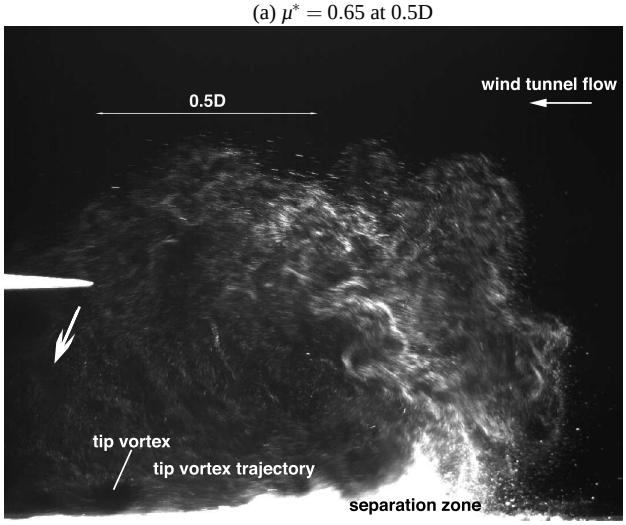

(b) $\mu^* = 0.37$ at 0.5D

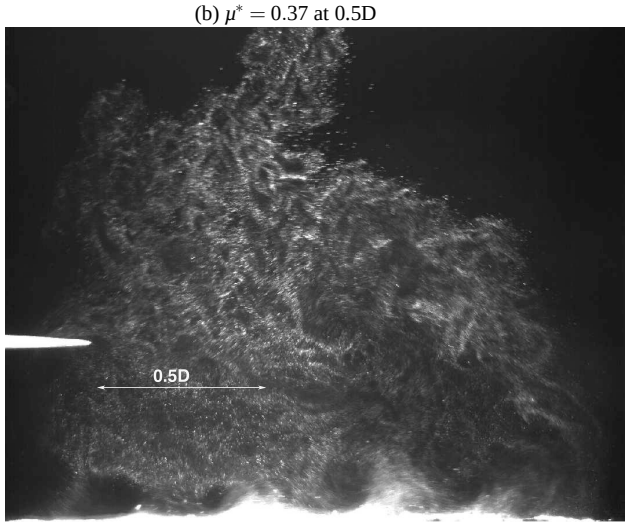

Figure 9: Stills from high speed video sequences of simulated brown-out using talcum powder spread over the tunnel floor. Rotor 0.5D above the ground. The leading edge of the rotor disk can be seen, and the wind tunnel flow is from right to left. A wider field of view was required for case (b).

to merge during hover). This sequence is thought to be the cause of the dust clouds occasionally extending to heights of around 1D, as shown in Figure 11(a). The lower forward flight speed,$\mu^\star = 0.37$, shows the changes in the cloud size more prominently. The difference in size of the cloud is comparable to the difference observed in the instantaneous vorticity plots obtained for the $\mu^\star = 0.3$ case from the PIV tests, as shown in Figures 11(a) and 11(b). Some of the tip vortices are seen to move towards the rotor disk to be re-ingested. Examples of this re-ingestion are shown in Figure 12. This is seen to be more obvious in the higher $\mu^\star$ case and is more frequently observed than the accumulation process at the lower rotor ground distance. The re-ingestion phenomenon is more clearly observed from the flow visualisation videos than the PIV plots. Figure 12, taken at the same μ^*, at different ground heights also show that the physical height of the mean dust clouds are similar (notwithstanding the occasions where the dust reaches heights above the rotor disk). Another major observation from the brown-out videos is the three dimensionality of the flow. Clouds of powder, originating from elsewhere in the flow can appear in the plane of view of the flow being monitored. Similarly, dust originating within the plane of view can be seen disappearing from view. This has been attributed to the strong cross-flow components present within the GE flow field.

3.3. Stereo PIV Results

The Stereo PIV results were used to investigate the cross-flow velocity components present in the GE flow field. Comparisons of the mean vorticity plots obtained from the Stereo PIV to those of the 2D PIV tests show good correlations. Figure 13 shows plots of mean vorticity and the corresponding cross-flow (w) velocity component for the cases where the rotor was at half a diameter above the ground and operating at $\mu^* = 0.4$ and $\mu^* = 0.6$. Analysis of the w-velocity contour plots show the presence of a region of negative cross-flow, just below the region of positive vorticity seen in the vorticity plot. This negative w component of velocity (flow into the page) is seen to exist ahead of the region of vorticity and form closer to the rotor tip, with increasing advance ratio. Just above this is a smaller region of positive (w) component (flow out of the page) of comparable magnitudes. The existence of cross-flow velocity components within the same vicinity of the flow indicates the strong 3-dimensionality of the ground effect flow field and requires further investigation.

Figure 14 shows the comparisons of the w velocity components for the range of μ^* tested at a rotor ground height of half a diameter. The images show the strengthening of the negative cross-flow along the ground as the μ^* increases. The regions dominated by the cross-flow are seen to reduce in size and concentrate around the disk leading edge, while increasing in strength. The presence of the outflow (positive w component) just ahead of the rotor disk comes as somewhat of a surprise due to the direction of blade movement (rotor rotating in the anti-clockwise sense, with the direction of blade movement into the page). This is worthy of further investigation.

4. DISCUSSION

Quantitative and qualitative data from experimental measurements of the flow around a rotor in ground effect in low speed forward flight have been presented. The rotor in these experiments was not trimmed in any way, but only gross effects of the flow field were under investigation during the experiments. The ground was also stationary relative to the rotor hub, and the flow simulation is therefore not truly representative of a rotor moving over a stationary ground in terms of kinematics. These are issues that can only be addressed using far more sophisticated experimental rigs. PIV was used to measure the velocity in selected areas around the rotor, and the magnification used allowed the image processing algorithms to produce high fidelity velocity maps. Velocity histograms are used in PIV to reveal systematic bias errors [17], and the only velocity clustering observed from the PIV results, tended to

(a) Start of sequence

(b) 2.8 revolutions after frame (a)

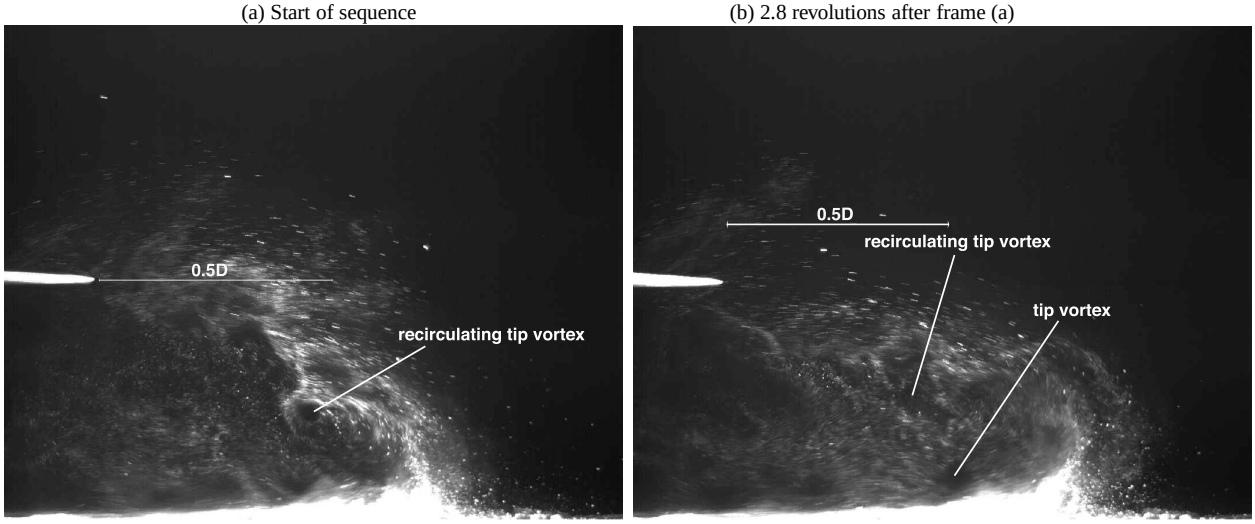

(c) 5.6 revolutions after frame (a)

(d) 8.5 revolutions after frame (a)

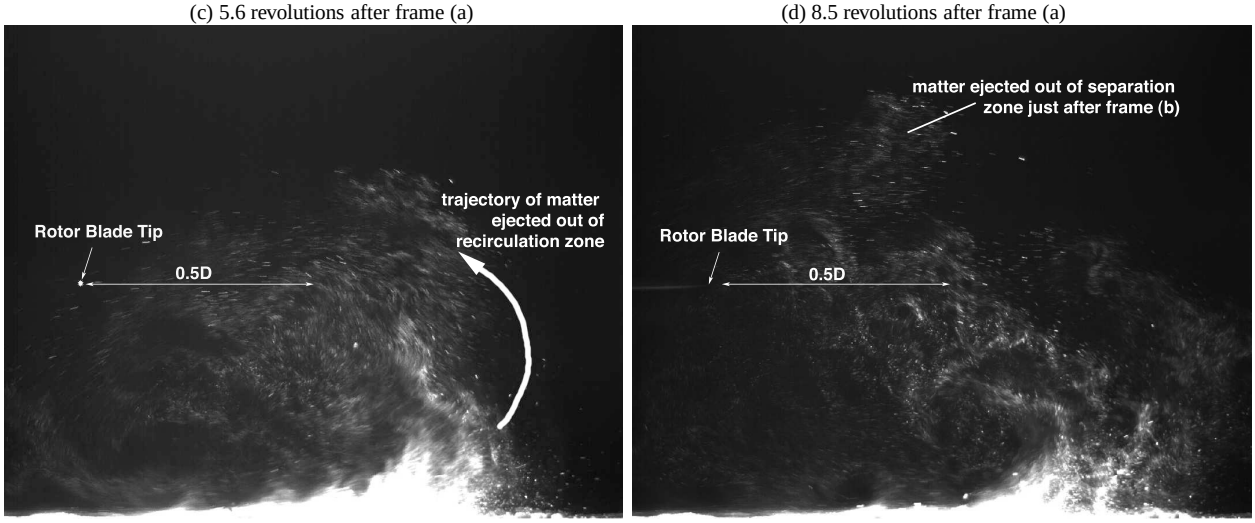

Figure 10: Stills from high speed video sequences of simulated brown-out using talcum powder spread over the tunnel floor for the rotor 0.5D above the ground, $\mu^* = 0.65$. The leading edge of the rotor disk can be seen, and the wind tunnel flow is from right to left.

(a) $\mu^* = 0.37$ at 0.5D

(b) $\mu^* = 0.3$ at 0.5D

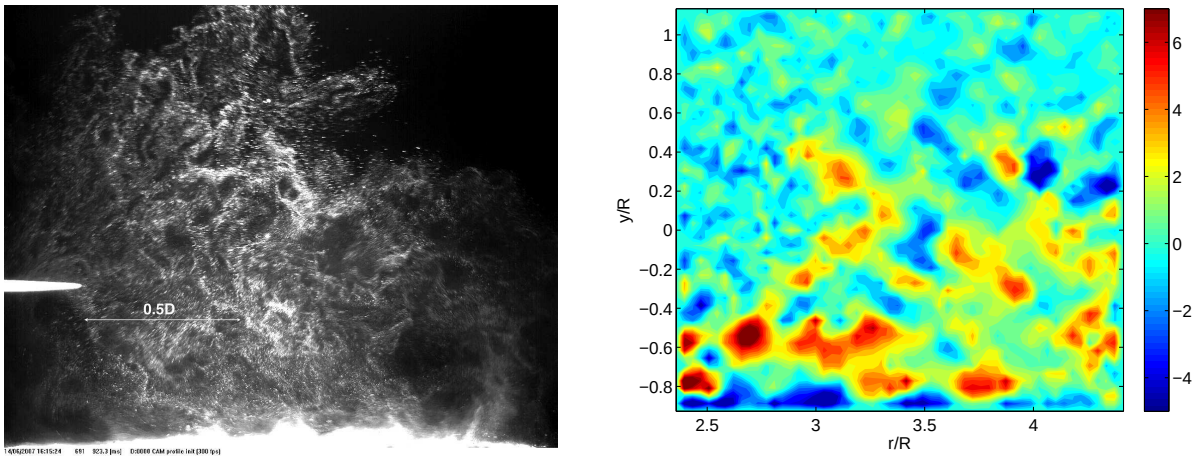

Figure 11: Figure shows the heights reached by the dust cloud and the positive vorticity in the brown-out and PIV tests. Frame (a) shows the rotor at $\mu^\star = 0.37$ and a ground distance of 0.5D. Frame (b) shows an instantaneous vorticity plot from PIV at $\mu^\star = 0.3$ and a ground distance of 0.5D.

(a) $\mu^* = 0.65$ at 0.5D

(b) $\mu^* = 0.65$ at 0.25D

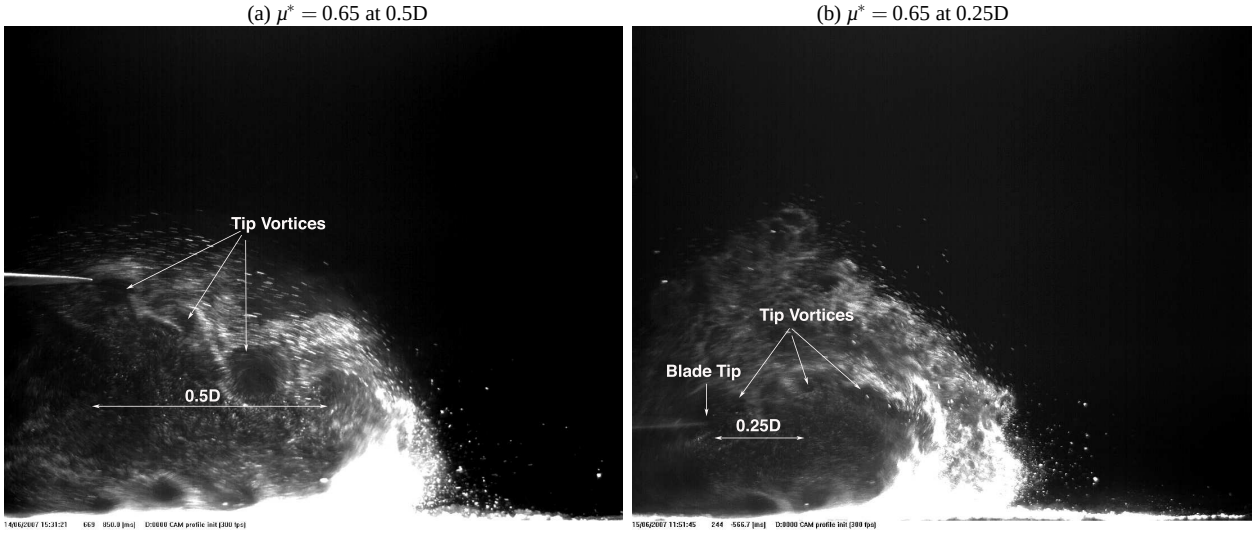

Figure 12: Stills from high speed video sequences of simulated brown-out. Rotor operating at $\mu^\star = 0.65$. Frame (a) shows the re-ingestion of the TVs at a ground distance of 0.5D while Frame (b) shows the re-ingestion at a ground distance of 0.25D.

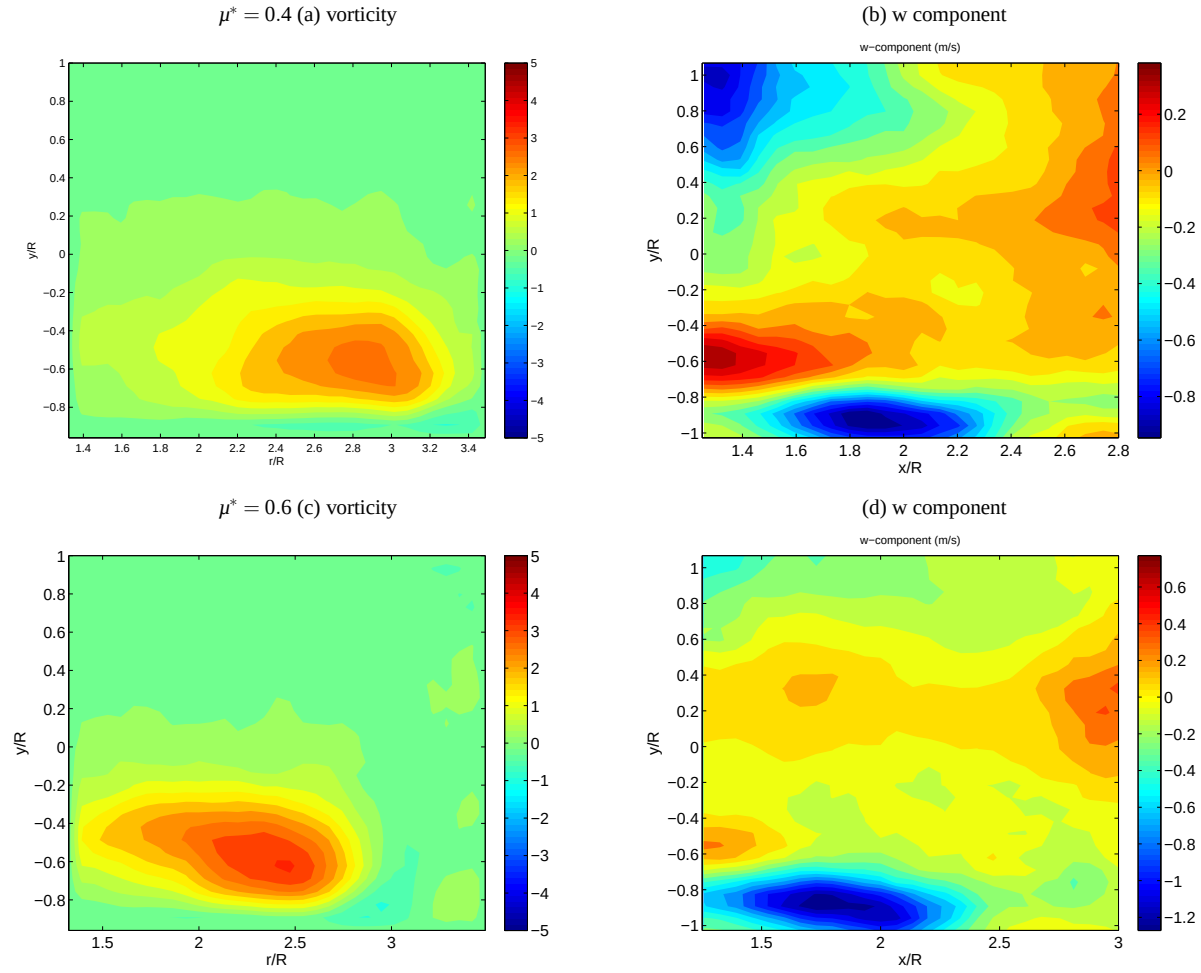

Figure 13: Mean Vorticity and mean cross-flow (w) velocity from Stereo PIV for the rotor at 0.5D above the ground for $\mu^* = 0.4$ and $\mu^* = 0.6$. For all the frames, the field of view is just upstream of the rotor tip.

(a) w component at $\mu^* = 0.3$

(b) w component at $\mu^* = 0.4$

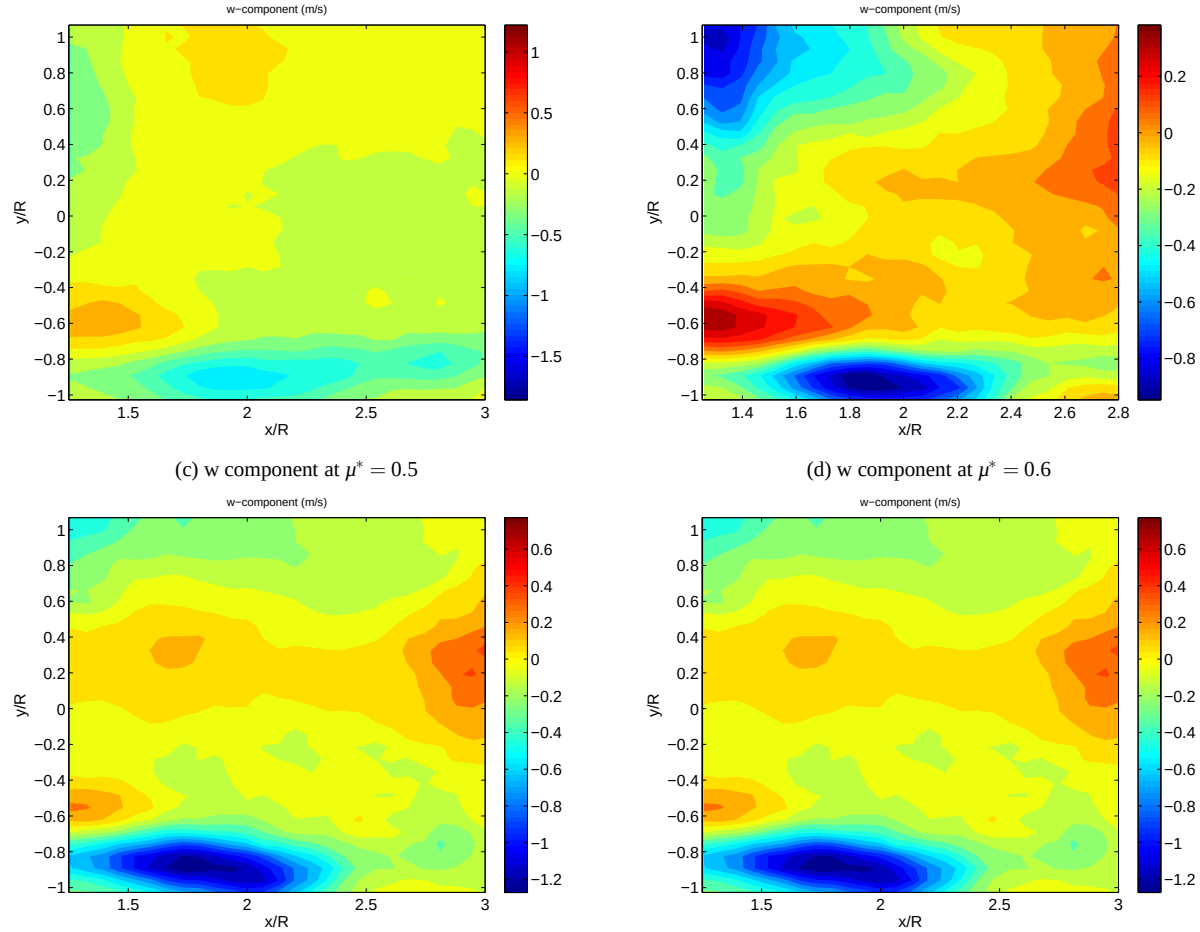

(c) w component at $\mu^* = 0.5$

(d) w component at $\mu^* = 0.6$

Figure 14: Mean cros- flow velocity (w) from Stereo PIV for the rotor at 0.5D above the ground for $\mu^* = 0.3$ tp $\mu^* = 0.6$. For all the frames, the field of view is just upstream of the rotor tip.

	Curtiss *et. al* [3] μ^*	**PIV Data** μ^*
Ground distance	0.45d	0.5d
Recirculation Regime	0.4 - 0.64	0.6 - 0.9
Ground Vortex Regime	0.64 - 0.83	0.9 - 1.1
	Ganesh *et. al* [14] μ	**PIV Data** μ
Ground distance	0.36d	0.5d
Recirculation Regime	0.03 - 0.05	0.044 - 0.07
Ground Vortex Regime	0.06 - 0.08	0.08 - 0.09

Table 2: Comparison of GE Data

occur around the imposed wind tunnel speed and around zero velocity (corresponding to masked out-of-bounds areas and low magnitude *u* and *v* components). This lack of clustering around other values of velocity indicates a well conditioned experiment and analysis for PIV. The brown-out simulations have proven to be a highly effective way of visualising the dust cloud generated by a rotor near the ground; the dust pick-up by the rotor flow and the subsequent evolution of the dust cloud can be seen.

A comparison of the PIV results with some previously done GE research is presented in Table 2. Similar μ^* values for the various GE flow regimes were obtained for comparable rotor ground distances by the PIV and research done by Ganesh *et. al*. [14]. Comparisons of the PIV results with the research by Curtiss *et. al* [3] showed greater differences in terms of the μ^* values at which different GE flow regimes were observed to occur. This difference is observed because of the inherent differences in the experimental conditions between the two sets of tests. While Curtiss *et. al* used a towing facility, with a helicopter model moving over ground, the PIV tests were conducted in a wind tunnel, with a stationary ground. The consequence of this is the presence of a ground boundary layer in all the experimental data obtained. It was important to ascertain the degree of influence of this boundary layer on the data obtained to determine if the analysis of the GE flow features were influenced by the presence of this boundary layer. Assuming that the ground board is a flat plate, the average boundary layer thickness at the various locations the rotor was placed on the ground board was calculated to be around 1cm; when scaled with respect to the rotor radius, this amounts to 0.15R. Considering that the ground board is located at $\frac{y}{R} = -1$ for the tests where the rotor ground distance was half a diameter and $\frac{y}{R} = -0.5$ for the cases where the rotor ground distance was a quarter of a diameter, it is unlikely that the gross features of the flow field were affected by the boundary layer. However, since it has not been possible to remove the effect of the boundary layer on the experimental data, direct comparisons with other GE research done in towing facilities or with a moving ground are difficult. The presence of the ground boundary layer presents a challenge for wind tunnel experimentation of ground effect in forward flight and is a topic worthy of further investigation.

To summarise the experimental results, it was observed that for a particular height, the PIV results show the presence of flow separation and a region of positive vorticity formed at the lowest forward flight speed tested ($\mu^\star$=0.3). This region of positive vorticity was seen to increase in strength and reduce in size with increasing $\mu^\star$, while forming nearer the rotor leading edge. Although the general flow features at $\mu^\star = 0.3$ and $\mu^\star = 0.65$ are similar, the two cases are considered to represent different regimes of the GE flow field due to the definitions of the GE regimes. This distinction within the flow field was made by considering the path taken by the TVs around the region of positive vorticity. Only when the TVs are re-ingested through the rotor, as shown in Figure 8, was the flow considered to be in the recirculation regime [3, 14]. Analysis of the individual vorticity plots of the GE flow field when the rotor is at a ground distance of half a diameter, operating at $\mu^\star = 0.3$, as shown in Figures 11(b), show the TVs accumulating around the zone of positive vorticity at around 3.6R, well away from the rotor. The TVs leaving the separation point of the ground are not seen to reach the rotor and hence not considered to be part of the recirculation flow regime, unlike the $\mu^\star = 0.65$ case, where the TVs are seen to reach the rotor disk.

For the current test conditions at least, a comparison of the PIV results and the brown-out tests shows that the main brown-out cloud extends at least as far forward as the mean vorticity below the rotor. This can be seen when comparing Figures 4 and 9. In Figure 4(b) the positive vorticity region extends as far forward as about $\frac{r}{R} = 2.6$, while in Figure 9(a) for the same $\mu^* = 0.65$, the cloud extends forward by just under 2R forward of the tip of the disk, equivalent to just under 3R from the hub. The equivalent values for $\mu^* = 0.3$ are 4.5R for the PIV vorticity (as shown in Figure 4(d)) and 3.8R for the brown-out (as shown in Figure 9(b)), although the brown-out test was conducted at the higher value of $\mu^* = 0.37$ where the dust cloud would be smaller. Inspection of the brown-out movie sequences shows that while dust clouds close to the ground show rotation corresponding to positive vorticity, those parts of the dust cloud high up above the ground show no preferred sense of rotation. The PIV shows only weak positive or negative vorticity extending far above the level of the rotor disk, but where the dust cloud extends the highest the vorticity (or at least the lateral component resolvable in these experiments) is of low magnitude and no preferred sign. Examples of this are shown in Figures 11, where the vorticity as shown in the PIV plot is of lower magnitudes, further off the ground.

Velocity fluctuations statistics are conveniently represented by the root-mean-square (RMS) velocity fluctuations about the mean, of the captured field of view from the PIV plots. These statistics provide the magnitudes of velocity fluctuations experienced within the field of view, and is a good indication of the relative unsteadiness of the flow. The RMS velocity plots for the GE flow, shown in Figure 15, show the unsteadiness of the GE wake at different forward flight speeds with a rotor ground height of half a diameter. Figure 15 shows the lower μ^* cases to possess lower velocity fluctuations compared with the GV regimes at the higher μ^* values. The velocity fluctuations are however seen to affect a greater proportion of the GE flow field at the lower μ^* values than the higher μ^* values, with the greatest magnitudes of the unsteadiness observed closer to the ground. The velocity fluctuations are seen to be of very low magnitudes above the rotor disk. In the GV regimes, the velocity fluctuations are seen to be

concentrated around the location of the GV, with the higher magnitude fluctuations confined to within the GV itself. The surrounding flow field is observed to possess very low velocity fluctuations, implying the GV regime to be the steadier regime when compared with the recirculation flow regime. Brown-out observations at $\mu^* = 0.37$, indicated the flow high above the disk to exhibit intermittency. This intermittency is not reflected in the RMS velocity plots. Examining the PIV velocity history at specific points in the flow, much like placing a hot-wire probe at a particular location, will allow this to be traced. In this case however, the fluctuation measurements will not be time-resolved, and the periodicity of the intermittency cannot be determined. An example of the velocity fluctuations experienced at a particular point in a ground effect flow field is shown in Figure 16. This plot shows the u and v velocity component fluctuations experienced at a point $\frac{r}{R} = 2$ and $\frac{y}{R} \approx 0.8$ in the flow field, with the rotor at a ground distance of half a diameter and operating at $\mu^* = 0.35$. This corresponds to the location where large dust clouds are observed in the brown-out visualisation, as shown in Figure 11(b). The figure shows occasional bursts of higher or low velocity relative to the mean. A comparison of the individual vorticity plots, corresponding to a mean velocity case and a large velocity deviation case is shown in Figure 17. The difference between the two frames is clear and at the stated location of $\frac{r}{R} = 2$ and $\frac{y}{R} \approx 0.8$, frame (a) shows the presence of high vorticity concentrations, while frame (b) shows no vorticity around that point. This is an indication of the unsteadiness observed at that point in the flow field at the mentioned test conditions and corresponds well to the observations of the occasional large dust clouds made during the brown-out tests.

The total integrated vorticity was calculated by considering both the positive and negative circulation of the flow near the ground. It was ensured that all the circulation associated with the GE flow was captured when calculating the integrated vorticity. Figure 18 shows the integrated vorticity calculated for the range of μ^* tested at a rotor ground distance of half a diameter. The positive integrated vorticity, associated with the region of positive vorticity is seen to be significantly higher than the negative integrated vorticity. This implies that the GE flow is dominated by the TV system of the rotor, with the root vortex system playing no significant role in any of the GE flow regimes. Furthermore, this validates the observation that the negative vorticity clusters observed in the individual vorticity plots from the PIV are due to the secondary separation caused by the TVs trailing along the ground. A comparison of the positive integrated vorticity, at the two primary ground heights tested are shown in Figure 19. The positive integrated vorticity shows a general trend of being the greatest at the recirculation regimes of the flow, when the region of positive vorticity is the furthest away from the rotor disk, at the various ground distances tested. As the μ^* increases and the recirculation becomes more compact, the integrated vorticity reduces until the GV regime is reached. The integrated vorticity is then seen to reduce at a slower rate in the GV regime until the GV disappears. Variations in the integrated vorticity at the higher rotor ground distances appear to be more pronounced than at the lower rotor ground distances. This differences can be clearly seen at the μ^* where the transition between the recirculation and the GV flow regimes occur. While the half a diameter ground distance results show a sudden drop in integrated vorticity, the results from the quarter of a diameter ground distance case appears to be more gradual.

Centroid locations of the regions of vorticity at each μ^* was computed for the different rotor ground distance cases. Figure 20 show the centroid locations in terms of the spanwise locations ($\frac{r}{R}$) and the heights of the centroids above the ground ($\frac{y}{R}$). A comparison of the spanwise centroid locations, in Figure 20(a), show the movement of the vorticity centroid towards the rotor disk with increasing μ^*. The difference in the spanwise locations between the different ground distances is seen to be greater at the higher μ^* values. At the μ^* where both the quarter and half a diameter ground distance cases are in the same flow regime; i.e. the recirculation regime, the spanwise locations of the centroids appear to be at a similar locations for similar values of μ^*. The vorticity is then seen to move closer to the rotor for the half a diameter ground distance case and go into the GV regime, while the quarter of a diameter ground distance case remains in the recirculation flow regime at comparable μ^*. The plots also suggest a more rapid change in the spanwise vorticity centroid locations at the higher ground distance compared to the lower ground distance, for the range of μ^* tested. Figure 20(b) indicate the heights to which the vorticity at the different ground distances reach at the various GE flow regimes. The figure indicates that within the same flow regimes, at the various ground distances, the heights of the vorticity centroids, are similar, for similar μ^*. The figure also indicates that within the recirculation flow regime, at a particular ground distance, the height of the centroid varies slightly, across the range of μ^*. This change in height, is once again, seen to be more obvious in the higher ground distance cases, than the lower ground distance cases. The plots however indicates the extent of influence the GE flow has on the entire flow field ahead of the rotor disk. This, together with the brown-out visualisations suggest that larger areas of the ground effect flow field has to be investigated further to comprehend the influence of the ground on the surrounding rotor flow.

5. CONCLUSION

An investigation of ground effect has been performed. The experiments conducted allowed for both qualitative and quantitative analysis of large areas of the ground effect flow field. Three-dimensional velocity, vorticity and RMS velocity fluctuation measurements permitted for the ground effect flow regimes to be characterised. Trends concerning the ground separation locations, circulation and vortex centroids at various rotor ground heights and normalised advance ratios were established from the PIV tests. Comparisons of the PIV data with other research showed good compatibility even though the experiments were conducted in a wind tunnel with a stationary ground. From the PIV tests, it was established that the recirculation regime consisted of a region of vorticity, spread over a relatively large distance of the flow along the ground. Re-ingestion of tip vortices was occasionally observed at the lower advance ratios of the recirculation regime, with the frequency increasing with increasing advance ratio and decreasing rotor ground distances. The ground vortex regime was observed to be more steady, with the unsteadiness confined

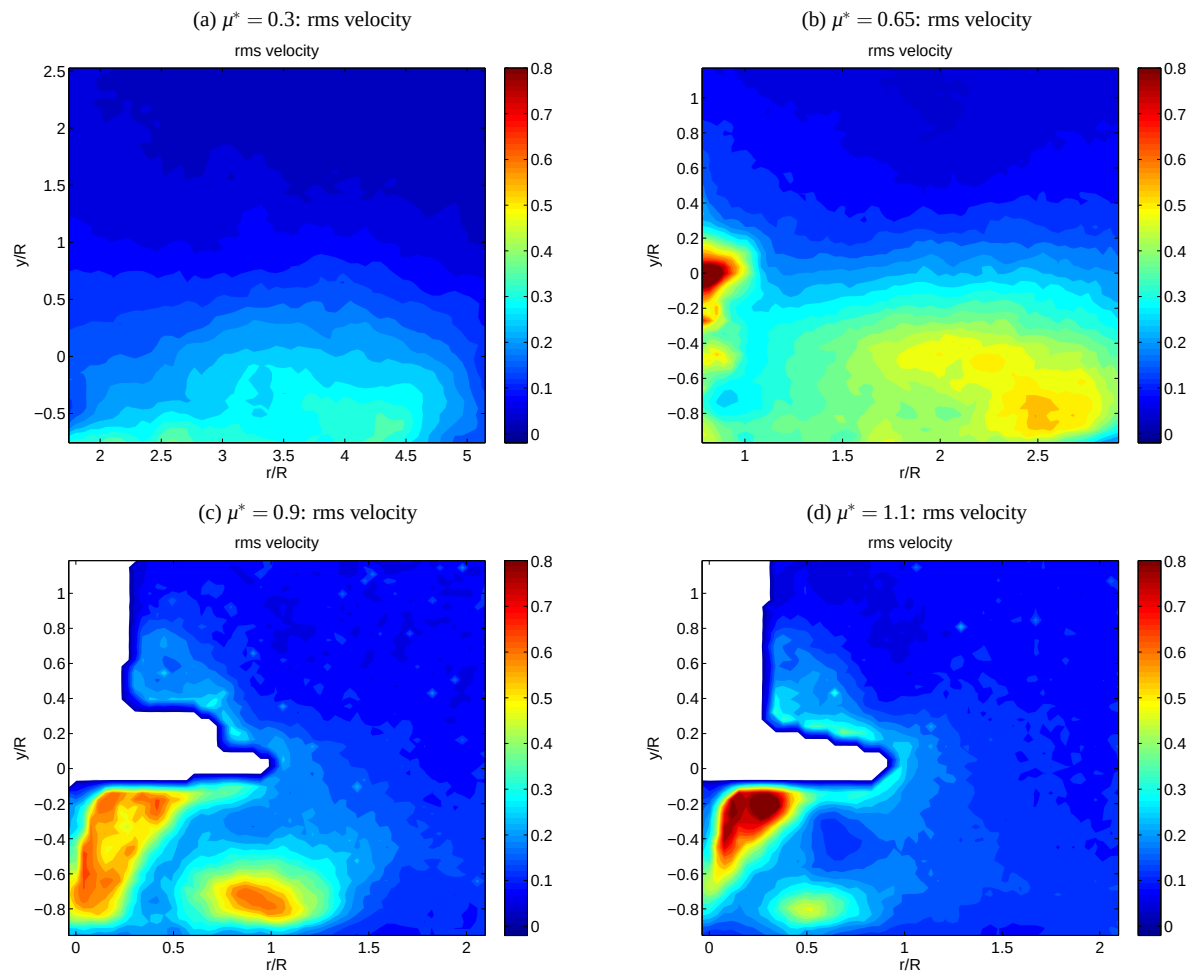

Figure 15: Root mean square velocity from PIV for the rotor at 0.5D above the ground for $\mu^* = 0.3$, $\mu^* = 0.65$, $\mu^* = 0.9$ and $\mu^* = 1.1$.

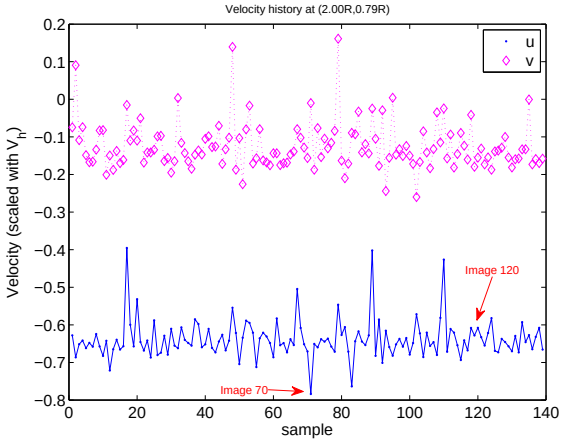

Figure 16: Velocity fluctuations at a point in the flow field for the case where the rotor is 0.5D above the ground with the flow at $\mu^* = 0.35$. The velocity fluctuations are measured at a point 2R from the rotor hub and a height of $\frac{y}{R} \approx 0.8$.

$\mu^* = 0.35$ (a) Image 70 at large fluctuation (b) Image 120 at mean velocity

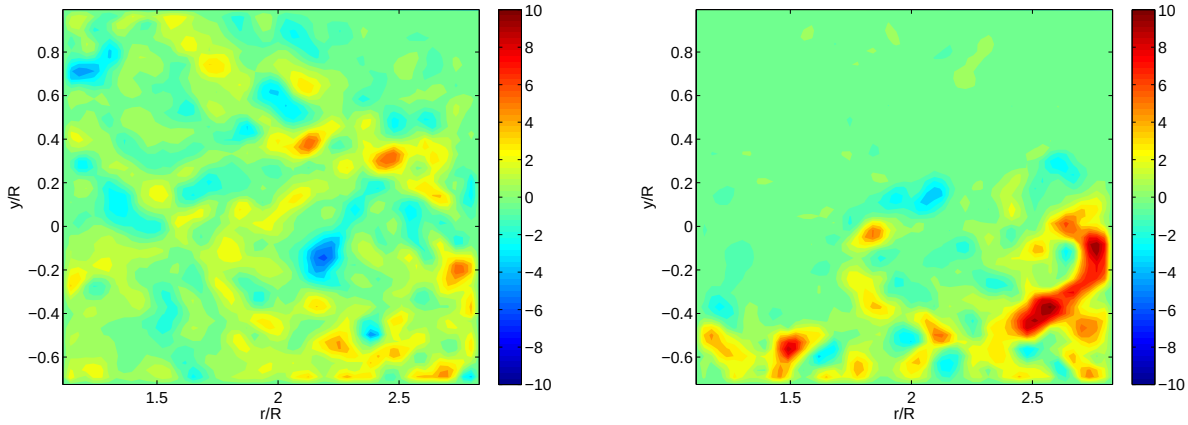

Figure 17: Individual PIV vorticity plots showing unsteadiness in the flow field at $\mu^* = 0.35$. Rotor at ground height of 0.5D Frame (a) shows a plot where the vorticity reaches the height of $\frac{y}{R} \approx 0.8$ while Frame (b) shows no vorticity at that height.

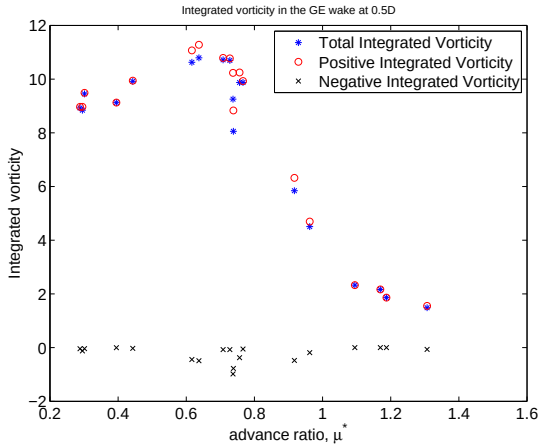

Figure 18: Integrated vorticity calculated at the various μ^*s tested for a rotor ground distance of 0.5D.

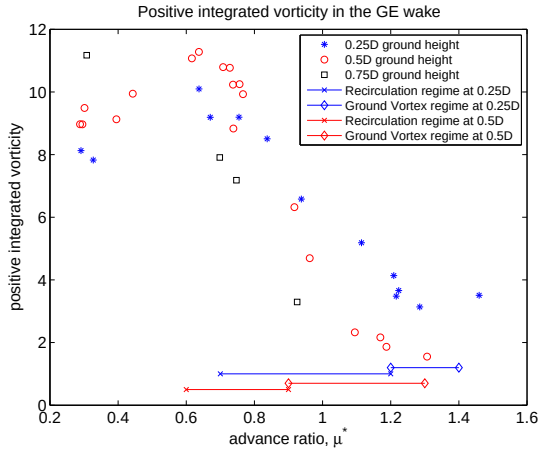

Figure 19: Positive Integrated vorticity calculated at the various μ^*s tested for the different ground distances.

(a) Spanwise location of vorticity centroids

(b) Height of vorticty centroids

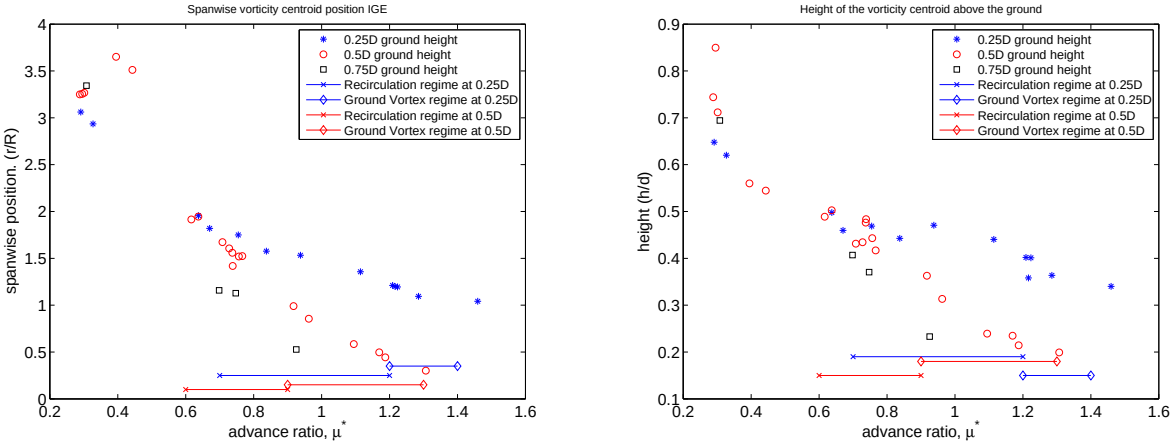

Figure 20: Location of the vorticity centroids at different ground distances for the range of μ^* tested. Frame (a) shows the spanwise location of the centroids and Frame (b) shows the height of the centroids relative to the ground.

to within the boundaries of the ground vortex.

The brown-out phenomenon, simulated in the wind tunnel showed the influence of the tip vortices on the dust cloud ahead of the rotor. At the normalised advance ratios tested, the tip vortices were either seen to accumulate ahead of the rotor disk, resulting in more powder to be picked up, building up the dust clouds to reach greater heights, or were observed to be re-ingested through the rotor disk. The unsteadiness of the recirculation regime was obvious with the movement of the separation zone along the ground. Comparisons of the brown-out and PIV tests show the dust cloud accumulating in the regions of high vorticity identified from the PIV plots, although the dust cloud is seen to reach greater heights than the region of strong, mean vorticity. The results presented in this paper have been obtained from tests which are not true experimental simulations of a rotor operating near the ground. The results have the effect of the ground boundary incorporated in them; whilst the boundary layer is not seen to affect the gross features of the flow field, which were investigated in this paper, more sophisticated experiments, with a moving ground and more advanced rotor rigs are necessary if a complete investigation of the rotor in ground effect flow is sought.

References

[1] J. Zbrozek. Ground effect on the lifting rotor. *British ARC*, R & M No. 2347, July 1947.

[2] E. A. Fradenburgh. The helicopter and the ground effect machine. *Journal of the American Helicopter Society*, 5(4):24, October 1960.

[3] H. C. Curtiss, M. Sun, W. F. Putman, and E. J. Hanker. Rotor aerodynamics in ground effect at low advance ratios. *Journal of the American Helicopter Society*, 29(1):48–55, 1984.

[4] J.G. Leishman. *Principles of helicopter aerodynamics, Second Edition*. Cambridge Aerospace Series. Cambridge University Press, Cambridge, UK, 2006.

[5] H. C. Curtiss, W. Erdman, and M. Sun. Ground effect aerodynamics. *Vertica*, 11(1-2):29–42, 1987.

[6] J.S. Hayden. The effect of the ground on helicopter hovering power required. *32nd Annual Forum of the American Helicopter Society*, May 1976.

[7] R.E. Brown and G.R. Whitehouse. Modelling rotor wakes in ground effect. *Journal of the American Helicopter Society*, 49(3):238–249, 2004.

[8] P. F. Sheridan and W. Wiesner. Aerodynamics of helicopter flight near the ground. In *33rd Annual Forum of the American Helicopter Society*, May 1977.

[9] B. A. Ganesh and N. Komerath. Unsteady aerodynamics of rotorcraft in ground effect. In *22nd Applied Aerodynamics Conference and Exhibit*, Providence, Rhode Island, 16-19 Aug 2004.

[10] D. Pulla and A. Conlisk. The long term structure of a rotor wake in ground effect. In *43rd AIAA Aerospace Sciences Meeting and Exhibit*, Reno, Nevada, January 2005.

[11] T. Saijo, B. Ganesh, A. Huang, and N. Komerath. Development of unsteadiness in a rotor wake in ground effect. In *21st AIAA Applied Aerodynamics Conference*, Orlando, Florida, June 2003.

[12] E.A. Boyd and I Kusmarwanto. Ground effect on a rotor wake. In *Cranfield Institue of Technology, College of Aeronautics, Report 8323*, 1983 1983.

[13] I. Kusmarwanto. *Ground Effect on a Rotor Wake*. PhD thesis, Cranfield Institute of Technology, College of Aeronautics, March 1985.

[14] B. A. Ganesh, N. Komerath, D. Pulla, and A. Conlisk. Unsteady aerodynamics of rotorcraft in ground effect. In *43rd Aerospace Sciences Meeting and Exhibit*, Reno, Nevada, January 2005.

[15] B. A. Ganesh and N. Komerath. Study of ground vortex structure of rotorcraft in ground effect at low advance ratios. In *24th Applied Aerodynamics Conference*, San Francisco, California, USA, 5-8 June 2006.

[16] A.K. Prasad. Stereoscopic particle image velocimetry. *Experiments in Fluids*, 29, February 2000.

[17] M. Raffel, C.E. Willert, and J. Kompenhans. *Particle Image Velocimetry. A practical guide*. Springer -Verlag Berlin Heidelberg, 1998.